ISIJ International, Vol. 65 (2025), No. 9, pp. 1339–1347
https://doi.org/10.2355/isijinternational.ISIJINT-2025-129

Achieving Remarkable Enhancement of Yield Strength Ensuring Large Ductility in a Metastable $Fe_{50}Mn_{30}Cr_{10}Co_{10}$ High-entropy Alloy via Warm Rolling Treatment

Xiaodong LAN,[1)*] Kaneaki TSUZAKI,[1,2)] Rintaro UEJI[1)] and Akinobu SHIBATA[1)]

1) Research Center for Structural Materials, National Institute for Materials Science, 1-2-1 Sengen, Tsukuba, Ibaraki, 305-0047 Japan.
2) Kyushu University, 744 Motooka, Nishi-ku, Fukuoka, 819-0395 Japan.

(*Received April 12, 2025; Accepted June 4, 2025; Advance online published June 16, 2025; Published August 15, 2025*)

The metastable $Fe_{50}Mn_{30}Cr_{10}Co_{10}$ (at.%) high-entropy alloy (HEA) integrates the principles of HEA and transformation-induced plasticity (TRIP), resulting in an exceptional combination of tensile strength and ductility. However, the inherently low yield strength restricts its application as a structural material. In this study, 50% warm rolling at 573 K was employed as a straightforward and cost-effective thermomechanical processing strategy to fabricate metastable $Fe_{50}Mn_{30}Cr_{10}Co_{10}$ HEA with enhanced yield strength while retaining large ductility. The mechanical responses and deformation behaviors of the metastable HEA were examined using room temperature tensile tests, along with postmortem X-ray diffraction (XRD) and electron backscatter diffraction (EBSD) analyses. Compared to the fully recrystallized counterparts, the warm-rolled specimens exhibited a threefold increase in yield strength while retaining substantial uniform elongation. The warm rolling treatment increased the mechanical stability of the austenitic phase against stress-assisted γ-ε martensitic transformation, shifting the yielding mechanism from martensitic transformation to dislocation slip, thereby enhancing the yield strength. Moreover, warm rolling completely suppressed the athermal γ-ε martensitic transformation even at 77 K, while the strain-induced γ-ε martensitic transformation remained pronounced at room temperature, contributing to the alloy's high strength and large ductility.

KEY WORDS: metastable high-entropy alloy; warm rolling; martensitic transformation; ε-TRIP effect; mechanical properties.

1. Introduction

The ever-increasing demand for strong and ductile metallic materials has been driving the development of more complex alloys and novel processing strategies.[1–5)] Unfortunately, high strength and large ductility are usually mutually exclusive.[6–10)] Over the past two decades, high-entropy alloys (HEAs) have drawn tremendous attention as they open an entirely new realm of compositional opportunities for designing novel materials with exceptional mechanical properties.[1,3,11,12)] Recently, the principles of HEA and transformation-induced plasticity (TRIP) were integrated by Li *et al.*[3,13)] by introducing non-equimolar compositions to reduce the stacking fault energy, and a metastable $Fe_{50}Mn_{30}Cr_{10}Co_{10}$ HEA with exceptional tensile strength and ductility due to ε-TRIP effect has been developed. It should be noted here that the ε-TRIP effect results from the ε-martensitic transformation from a face-centered cubic (FCC) structure to a hexagonal close-packed structure (HCP), and not from α'-martensitic transformation from an FCC to a body-centered cubic (BCC) structure. This metastable HEA holds great potential for overcoming the strength–ductility trade-off by combining the extensive solid-solution strengthening characteristic of HEAs with the TRIP effect commonly observed in certain high-strength steels.[14–16)] However, the low yield strength (usually ~200–300 MPa at room temperature[3,13,17,18)]) restricts its application as a structural material. Compared with the high tensile strength and large ductility, attempts to simultaneously enhance the yield strength are still lacking.

According to the Hall–Petch relationship,[19,20)] grain refinement can effectively enhance the yield strength of polycrystalline materials. However, in the metastable HEA, Li *et al.*[13)] demonstrated a distinct behavior: refining grains from 45 μm to 4.5 μm simultaneously improved the tensile strength and ductility but resulted in only a minimal

* Corresponding author: E-mail: LAN.Xiaodong@nims.go.jp

increase in yield strength (~250 MPa to ~330 MPa), much smaller than the nearly twofold increase observed in a stable CoCrFeMnNi HEA.[21] This could be attributed to the fact that the metastable HEA yields via stress-assisted γ-ε martensitic transformation rather than dislocation slip in the austenite phase. Li *et al.*[22] further attempted to enhance the yield strength by adding interstitial carbon into the metastable HEA. Although the addition of carbon slightly improves the yield strength, it degrades the metastability-driven TRIP effect by enhancing the phase stability of austenite. Developing cost-effective and scalable processing strategies using conventional industrial technologies to achieve exceptional mechanical performance remains a key challenge.

In general, increasing the yield strength of stable FCC/BCC alloys (in which dislocation slip governs deformation) via conventional methods, such as grain refinement and work hardening, easily leads to a decrease in ductility because of a lack of work-hardening capability.[7,23,24] However, as an alternative deformation mode, deformation-induced martensitic transformation activated during deformation can enhance and regenerate work hardening, resulting in high strength and large ductility.[3,13,15,25] Olson and Cohen[26] classified the deformation-induced martensitic transformation into stress-assisted and strain-induced transformation, as illustrated in **Fig. 1**. At temperatures below M_s^σ, stress-assisted martensitic transformation is triggered by applied stresses lower than the typical yield stress of austenite (as extrapolated from higher to lower temperatures), leading to transformation-induced yielding. To achieve a metastable HEA with enhanced yield strength while retaining large ductility, it is essential to suppress the stress-assisted γ-ε martensitic transformation and keep the strain-induced γ-ε martensitic transformation at the later stage of deformation. By doing so, it is expected that yield strength can be enhanced without significantly sacrificing work-hardening capacity and ductility in the metastable HEA, through the activation of ε-TRIP effect. However, how to concurrently apply these two approaches and the underlying mechanisms that enable such behaviors remain unexplored. This study utilizes warm rolling above the M_d temperature: the metastable austenite is anticipated to be work-hardened and mechanically stabilized, switching the yielding mechanism from stress-assisted γ-ε martensitic transformation to dislocation slip and keeping ε-TRIP effect after austenite yielding. This novel approach, achieved through a conventional rolling process, further expands the design space for metastable HEAs by exploiting the tunable stability of the austenite phase. Therefore, the aim of this study is to elucidate the influence of warm rolling treatment on the mechanical properties of the metastable HEA and the ε-TRIP effect.

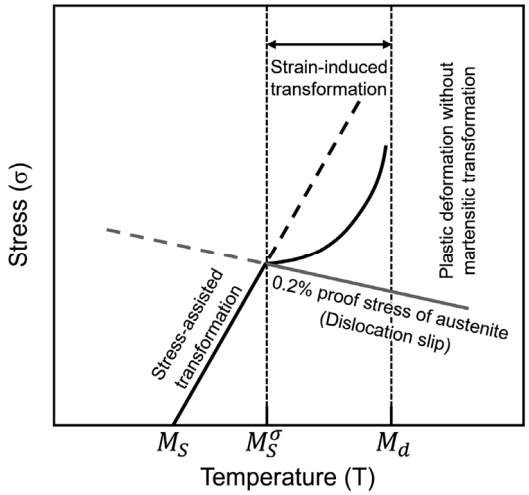

Fig. 1. Schematic illustration of critical stress to initiate martensitic transformation as a function of temperature, according to Olson and Cohen.[26]

2. Experimental Procedure

In this study, an ingot with nominal chemical composition of $Fe_{50}Mn_{30}Cr_{10}Co_{10}$ (at.%) was cast by vacuum induction melting. The detailed chemical composition is listed in **Table 1**. The as-cast ingot was hot rolled with a thickness reduction of 52% at 1 273 K followed by homogenization at 1 473 K for 2 h in an Ar atmosphere and furnace cooling. The homogenized plate was further hot rolled (HR) to obtain a thickness reduction to 33% (from 60 to 20 mm) at 1 273 K. The HR plate served as the starting material in this study and was processed via two distinct processing routes, as schematically illustrated in **Fig. 2**. In route (a), the HR plate with a thickness of 20 mm was annealed at 1 273 K for 1 h and then water-quenched to obtain a fully recrystallized austenite grain structure, hereafter referred to as ANN. The ANN plate was then warm rolled at 573 K to achieve a 50% reduction in thickness and subsequently water-quenched to attain a work-hardened austenite structure, denoted as ANN+WR. In route (b), the HR plate was directly warm rolled at 573 K to achieve a 50% reduction in thickness, followed by water quenching, resulting in another work-hardened austenite structure referred to as HR+WR. It should be noted that 573 K exceeds the A_f temperature

Table 1. Chemical composition of the metastable HEA (wt.%).

Fe	Mn	Cr	Co	Ni	C	N	O	Al	P	S
50.37	29.8	9.29	10.46	0.01	0.009	0.0087	0.015	0.028	0.004	0.007

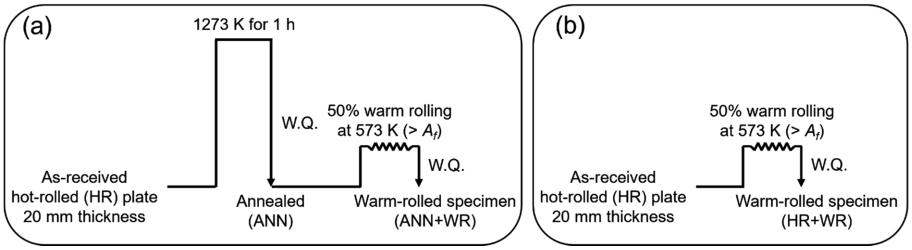

Fig. 2. Schematic illustrations of the thermomechanical processing routes.

(Koyama *et al.*[27]) reported that the M_s, A_s, and A_f temperatures were 328 K, 406 K, and 425 K, respectively) and thus the austenite phase is stable during warm rolling.

The microstructures of the HR, ANN, ANN+WR, and HR+WR specimens were examined using electron backscatter diffraction (EBSD). Two scanning electron microscopes (ZEISS Sigma and JEOL 7000F), equipped with a Bruker QUANTAX EBSD system and a TSL OIM EBSD system, respectively, were utilized. The EBSD measurements were conducted at an acceleration voltage of 20 kV with a beam step size of 0.4 μm. Analysis on the obtained EBSD data was performed using the Bruker QUANTAX ESPRIT software and the TSL OIM analysis software.

Sheet-type tensile specimens (20 mm × 4 mm × 2 mm, corresponding to length, width, and thickness, respectively) were machined from the HR, ANN, ANN+WR, and HR+WR plates via electrical discharge machining along the rolling direction (RD). Tensile tests were performed at room temperature with an initial strain rate of 1×10^{-3} s^{-1}. The tensile elongation was accurately measured using a strain gauge. To ensure reliability and reproducibility, two tensile specimens for each condition were tested. The mechanical responses and deformation behaviors were examined by combining tensile tests with postmortem X-ray diffraction (XRD) and EBSD analyses. XRD measurements were conducted using a Rigaku SmartLab diffractometer with Cu Kα radiation (λ = 0.15418 nm), operating at 45 kV and 200 mA. The measurements were carried out over a 2θ range of 5° to 140° with a step size of 0.02°.

Prior to the above EBSD and XRD measurements, the specimens were mechanically polished using silicon carbide grinding papers from 1 200 to 4 000 grit, followed by polishing with 3 and 1 μm diamond suspensions. Subsequently, fine polishing with 0.02 μm colloidal silica for more than 20 min was performed to effectively remove the deformation layer caused by mechanical grinding. Finally, the specimens were electrolytically polished in an electrolyte composed of 10% $HClO_4$ and 90% CH_3CH_2OH at 30 V for 60 s to completely remove the surface martensite induced by mechanical polishing.

3. Results and Discussion

3.1. Initial Microstructures

Figure 3 shows (a_1, b_1, c_1, d_1) the EBSD inverse pole figure (IPF) maps, (a_2, b_2, c_2, d_2) image quality (IQ) + phase maps, and (a_3, b_3, c_3, d_3) kernel average misorientation (KAM) maps of the (a_1–a_3) HR, (b_1–b_3) ANN, (c_1–c_3) ANN+WR,

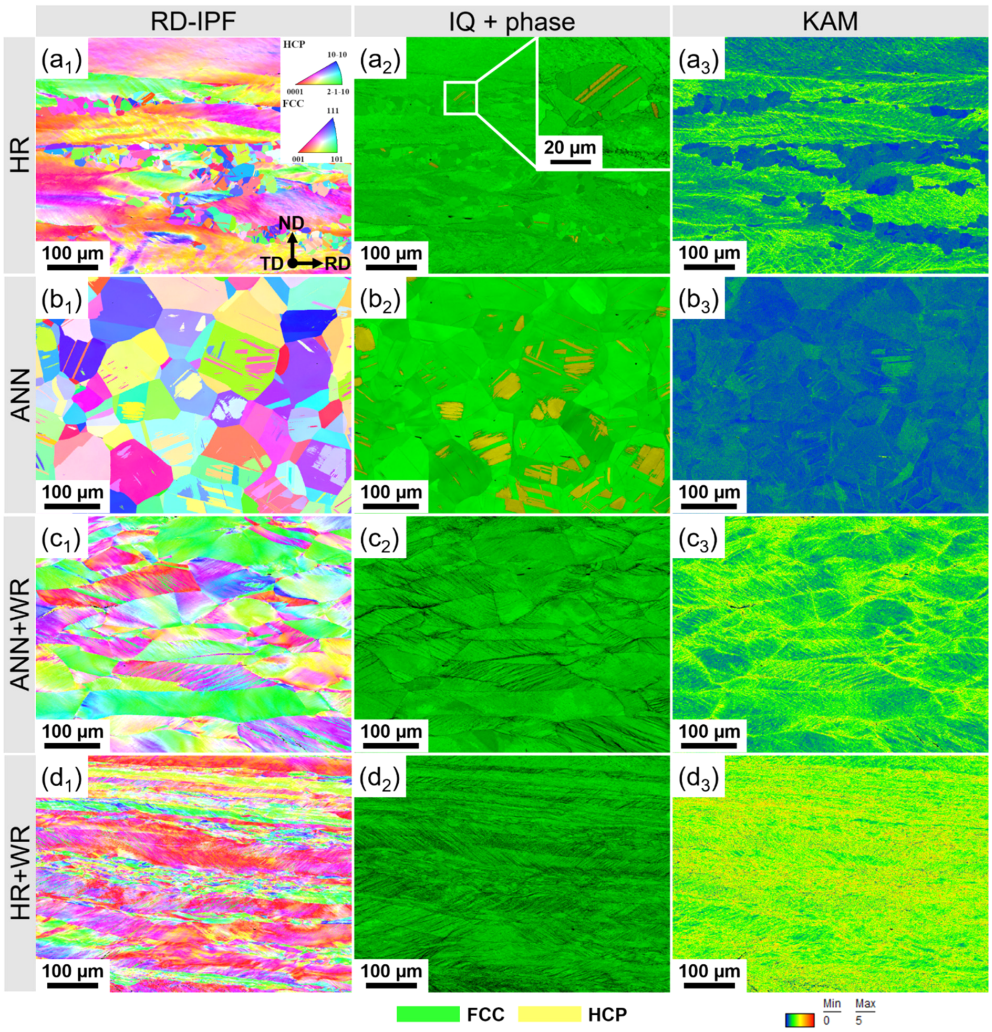

Fig. 3. Initial microstructures of the HR, ANN, ANN+WR, and HR+WR specimens before tensile deformation. (a_1, b_1, c_1, d_1) RD-IPF maps, (a_2, b_2, c_2, d_2) IQ + phase maps, and (a_3, b_3, c_3, d_3) KAM maps. ND: normal direction; RD: rolling direction; TD: transverse direction. (Online version in color.)

and (d_1–d_3) HR+WR specimens. The colors in the IPF maps represent the crystallographic orientations parallel to the RD as indicated by the stereographic triangle. As shown in Figs. 3(a_1)–3(a_2), the HR specimen shows a heterogeneous microstructure consisting of a partially recrystallized austenite grain structure (γ, FCC) and a small number of martensite plates (ε, HCP). The ε-martensite plates are detected in the recrystallized austenite grains, as shown in the inset of Fig. 3(a_2), whereas the non-recrystallized regions exhibit a single-phase austenite structure with relatively higher KAM values (see Fig. 3(a_3)). Figures 3(b_1)–3(b_2) reveals that the ANN specimen consists of a fully recrystallized austenite structure with a grain size of approximately 90 μm (excluding annealing twin boundaries) and athermal ε-martensite plates with a volume fraction of 10.4%. The ANN+WR specimen shows a deformed austenite structure, with no presence of ε-martensite, as illustrated in Figs. 3(c_1)–3(c_2). Similarly, the HR+WR specimen displays a deformed, heterogeneous single-phase austenite structure, as depicted in Figs. 3(d_1)–3(d_2). Both the ANN+WR and HR+WR specimens exhibit a single-phase austenite structure. The enhanced phase stability is attributed to the high dislocation density induced by warm rolling treatment. This is evidenced by the higher KAM values in Figs. 3(c_3) and 3(d_3), where elevated KAM correlates with a greater dislocation density.

3.2. Mechanical Properties

Figure 4(a) shows the representative nominal stress–strain curves of the HR, ANN, ANN+WR, and HR+WR specimens. The detailed tensile properties are summarized in **Table 2**. The ANN specimen exhibits a yield strength (YS, 0.2% offset) of 154.5±5.5 MPa, an ultimate tensile strength (UTS) of 678.5±0.5 MPa, a uniform elongation (UE) of 0.6±0.01, and a total elongation (TE) of 0.655±0.015. Interestingly, the HR specimen demonstrates better tensile properties (YS: 221±8 MPa, UTS: 683±2 MPa, UE: 0.6±0.01, TE: 0.68±0.03) compared to the ANN specimen, although a detailed investigation of this behavior is beyond the scope of this study. Compared to the ANN specimen, the YS of the ANN+WR specimen increases by almost threefold (154.5±5.5 MPa → 600±3 MPa), while maintaining a substantial UE of 0.34±0.01. Furthermore, the UTS (820±4 MPa) of the ANN+WR specimen is also significantly higher than that of both the HR and ANN specimens. An excellent combination of strength and ductility is achieved in the ANN+WR specimens. Notably, the HR+WR specimen exhibits a mechanical response almost identical to that of the ANN+WR specimen, despite significant differences in their initial microstructures. Figure 4(b) presents the corresponding true stress-strain curves and work-hardening rate curves for the metastable HEA specimens. While the HR+WR and ANN+WR specimens show a lower work-hardening rate during the intermediate and later stages of tensile deformation than the HR and ANN specimens, their absolute work-hardening capacity remains high. This exceptional work-hardening ability of the HR+WR and ANN+WR specimens effectively postpones the onset of necking instability, thereby enhancing the yield strength while preserving substantial ductility.

The excellent combination of yield strength and ductility achieved in the 50% warm-rolled metastable HEA is particularly noteworthy when compared to pre-deformed stable $Fe_{20}Mn_{20}Ni_{20}Cr_{20}Co_{20}$ (at.%) HEA. Zhao *et al.*[24] reported that a 40% cold rolling treatment significantly improved the yield strength of the stable $Fe_{20}Mn_{20}Ni_{20}Cr_{20}Co_{20}$ HEA. However, the plastic instability occurred immediately after yielding, resulting in a very limited uniform elongation, which is the usual case for heavily deformed metallic materials due to a lack of work-hardening capability. Therefore, the remarkable enhancement of yield strength coupled with large ductility achieved in the present metastable HEA is unusual, considering that it is in as-rolled condition with high initial dislocation density. The differences in the mechanical response between metastable and stable HEAs raise several important

Table 2. Mechanical properties of the HR, HR+WR, ANN, and ANN+WR specimens.

Specimen	YS (MPa)	UTS (MPa)	UE	TE
HR-1	229	685	0.61	0.71
HR-2	213	681	0.59	0.65
HR+WR-1	621	820	0.35	0.42
HR+WR-2	622	811	0.31	0.38
ANN-1	149	679	0.59	0.64
ANN-2	160	678	0.61	0.67
ANN+WR-1	597	816	0.35	0.43
ANN+WR-2	603	824	0.33	0.39

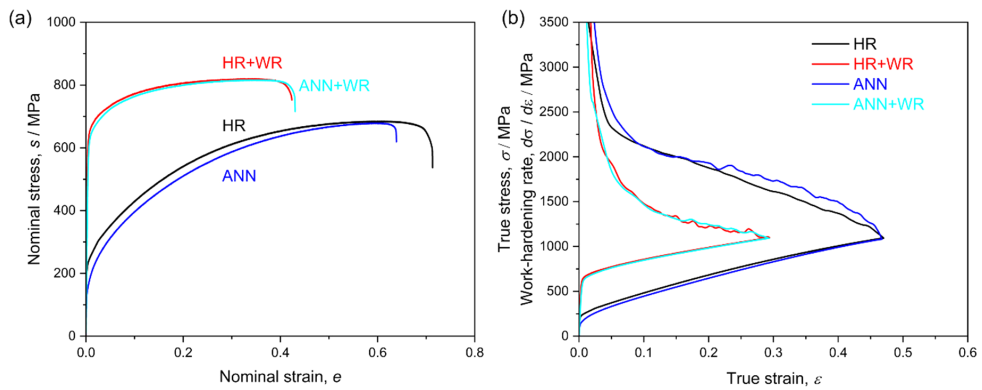

Fig. 4. (a) Nominal stress–strain curves of the HR, ANN, ANN+WR, and HR+WR specimens at room temperature; (b) True stress–strain curves and corresponding work-hardening rate curves. (Online version in color.)

issues that will be addressed in the following sections: (I) the γ-ε martensitic transformation progress in the HR+WR and ANN+WR specimens, (II) the influence of warm rolling treatment on ε-TRIP effect, and (III) the yielding mechanism in the HR+WR and ANN+WR specimens.

3.3. Deformed Microstructures

To elucidate the underlying deformation mechanisms responsible for the high yield strength and large ductility in the HR+WR and ANN+WR specimens, the deformed microstructures were analyzed at a tensile strain of 15% using EBSD. For comparison, the deformed microstructure of the ANN specimen was also examined at the same strain level. **Figure 5** shows the RD-IPF maps and corresponding IQ + phase maps depicting the deformation microstructures in the ANN, ANN+WR, and HR+WR specimens. As shown in Figs. 5(a_2)–5(c_2), both FCC γ and HCP ε phases are present in all specimens. The ε-martensite fraction in the ANN specimen increased from 10.4% to 40% after 15% tensile strain based on EBSD measurements. It is notable that the ε-martensite fractions in the ANN+WR and HR+WR specimens after 15% tensile strain were 25% and 24%, respectively. It has been confirmed that the initial microstructure of both the ANN+WR and HR+WR specimens shows a single-phase austenite structure. Hence, intensive deformation-induced γ-ε martensitic transformation also occurred in both the HR+WR and ANN+WR specimens. This could be the reason for the excellent work-hardening ability observed in those specimens. Additionally, the average thickness of ε-martensite plates in the HR+WR and ANN+WR specimens is significantly reduced compared to that in the ANN specimen. This reduction in thickness of ε-martensite plates can be attributed to the dislocations introduced by the warm rolling process, which increases the critical shear stress required for the movement of transformation dislocations, thereby hindering the thickening of ε-martensite plates. Nevertheless, deformation-induced γ-ε martensitic transformation can still proceed under high applied stress.

3.4. Contribution of TRIP Effect

To investigate the progression of the γ-ε transformation during deformation, the ANN, ANN+WR, and HR+WR specimens were analyzed using XRD at three deformation stages: before deformation, at 15% strain, and after fracture (non-necking area). **Figure 6** presents the XRD profiles of the ANN, ANN+WR, and HR+WR specimens

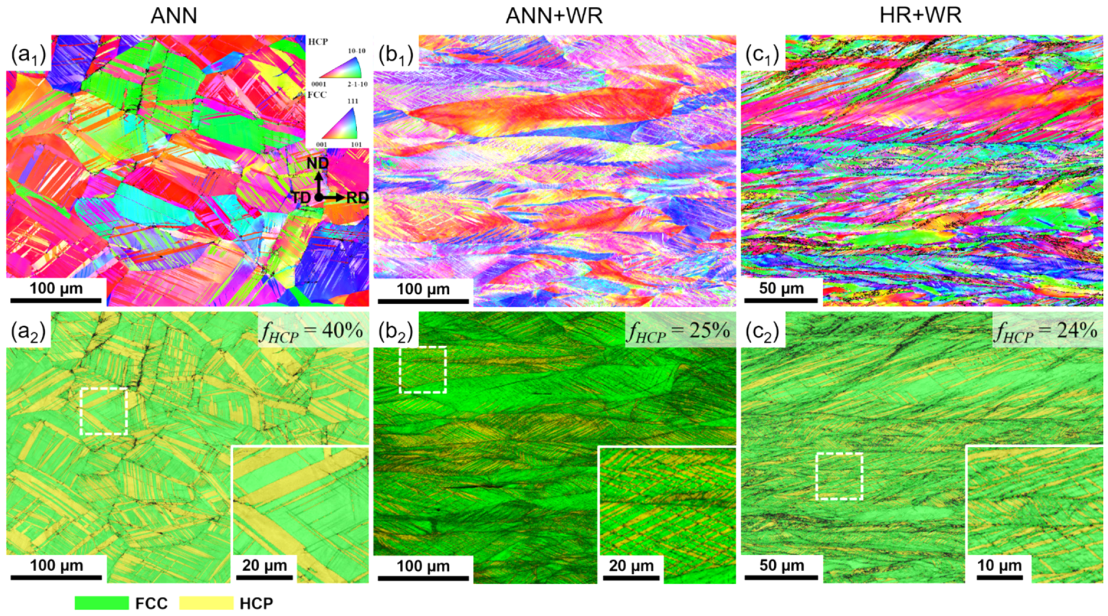

Fig. 5. Deformed microstructures of the (a_1, a_2) ANN specimen, (b_1, b_2) ANN+WR specimen, and (c_1, c_2) HR+WR specimen at a global strain level of 15%. (a_1, b_1, c_1) RD-IPF maps; (a_2, b_2, c_2) IQ + phase maps. (Online version in color.)

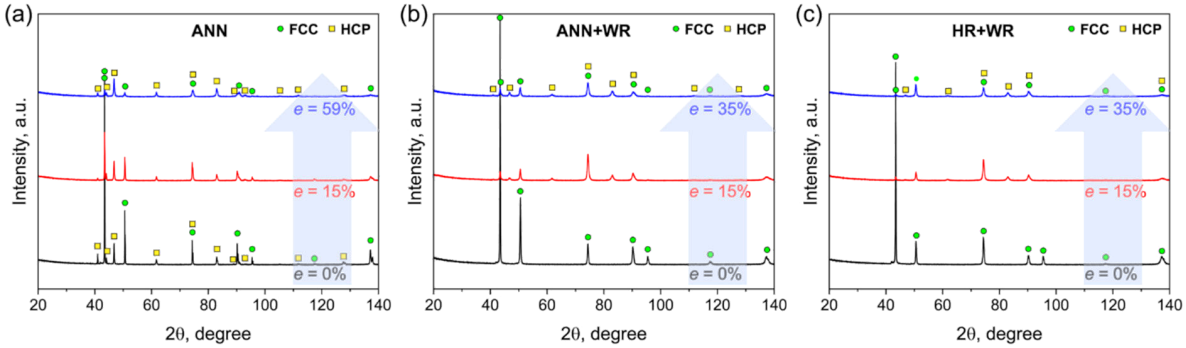

Fig. 6. XRD profiles of the (a) ANN specimen, (b) ANN+WR specimen, and (c) HR+WR specimen at various strain levels. (Online version in color.)

acquired at the aforementioned stages. As shown in Fig. 6(a), both athermal ε-martensite and FCC austenite were detected in the undeformed ANN specimen. In contrast, the XRD profiles for the ANN+WR (Fig. 6(b)) and HR+WR (Fig. 6(c)) specimens reveal a single-phase FCC structure before tensile deformation. These results are consistent with the EBSD analysis presented in Fig. 3. The diffraction peaks corresponding to ε-martensite developed during deformation, and the peak intensities increased gradually as the deformation progressed, indicating an increase in the ε-martensite volume fractions for all specimens. Furthermore, the lattice parameters of the ε-martensite were also retrieved by Rietveld analysis on XRD profiles. The result reveals a significantly reduced c/a ratio of 1.619 compared to the ideal value of 1.633. This modest change in the c/a ratio promotes the activation of non-basal slip and frequent cross slip,[28] which contributes to the high deformability of ε-martensite. The ε-martensite in the metastable HEAs has been observed to play a crucial role in plastic accommodation and work hardening at later deformation stages via multiple deformation mechanisms—including dislocation slip, formation of stacking faults, and mechanical twinning[13,29]—which significantly contributes to the overall strength and ductility. Consequently, the unexpectedly large elongation observed in the ANN+WR and HR+WR specimens can be attributed to the ε-TRIP effect and the intrinsic ductility of ε-martensite.

The evolution of the ε-martensite fraction in the metastable HEA during the above-mentioned deformation stages was quantitatively analyzed through EBSD measurements, as shown in **Fig. 7**. The blue, cyan, and red symbols represent the ANN, ANN+WR and HR+WR specimens, respectively. As strain increases, the γ-ε martensitic transformation progresses equally in the ANN+WR and HR+WR specimens, as in the ANN specimen. It is noteworthy that ε-TRIP effect occurs effectively even in work-hardened austenite. However, the transformation rate in the WR specimens is slightly slower than in the ANN specimen. After fracture, the volume fractions of ε-martensite (non-necking area) were measured as 74%, 42.2%, and 39.3% for the ANN, ANN+WR, and HR+WR specimens, respectively. By subtracting the initial athermal ε-martensite, the deformation-induced ε-martensite fractions were calculated as 63.6%, 42.2%, and 39.3%, respectively. These results indicate that both the transformation kinetics and the overall extent of deformation-induced martensitic transformation are reduced by the warm rolling treatment. This brings us to another issue to consider: the influence of warm rolling treatment on the austenite phase stability, which remains insufficiently understood and requires further investigation.

3.5. Stability of γ-ε Martensitic Transformation

The stability of metastable austenite is typically assessed through its thermal and mechanical stability. **Figure 8** shows

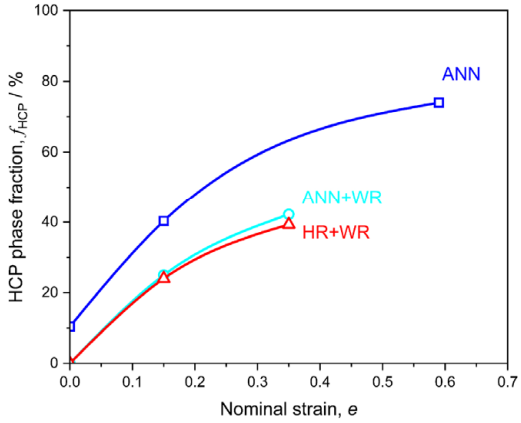

Fig. 7. Evolution of the ε-martensite fractions in the ANN, ANN+WR, and HR+WR specimens at various strain levels obtained by EBSD analysis. (Online version in color.)

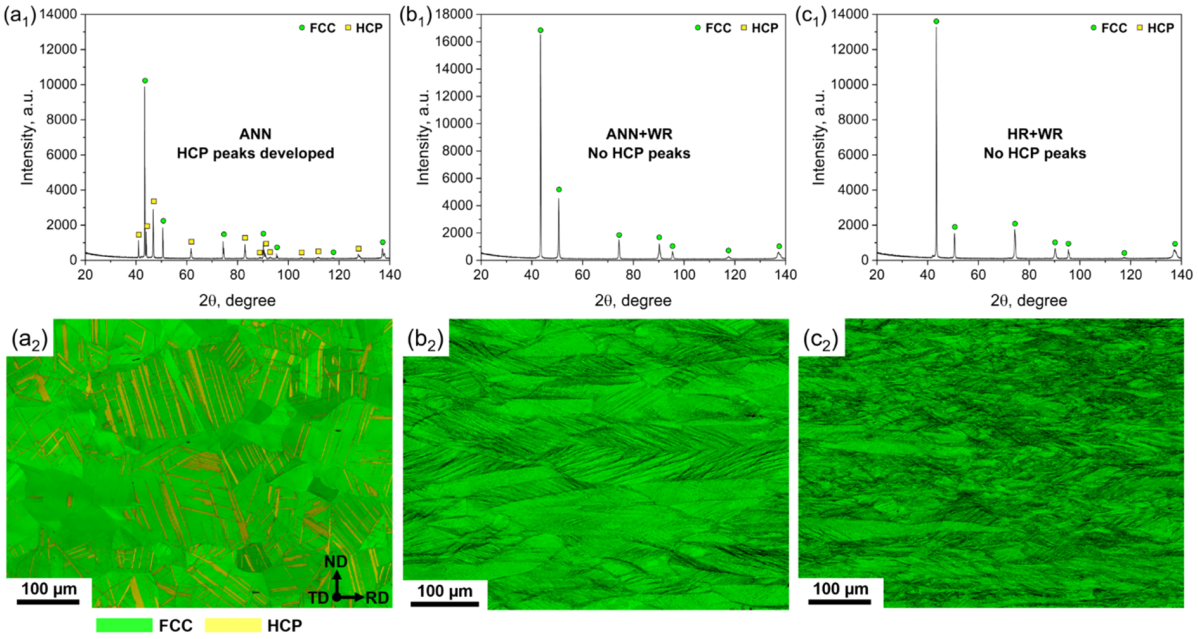

Fig. 8. (a_1), (b_1) and (c_1) are XRD profiles for the ANN specimen, ANN+WR specimen, and HR+WR specimen after subzero cooling to 77 K for 10 min, respectively; (a_2), (b_2) and (c_2) are the corresponding IQ + phase maps, respectively. (Online version in color.)

the XRD profiles and corresponding IQ + phase maps for the ANN, ANN+WR, and HR+WR specimens after sub-zero treatment at 77 K for 10 min. The ANN specimen exhibited an increased fraction of athermal ε-martensite, as confirmed by both XRD and EBSD analyses (see Figs. 8(a_1) and 8(a_2)). In contrast, the ANN+WR and HR+WR specimens maintained a single-phase austenite structure, indicating superior thermal stability. These findings demonstrate that the thermal stability of austenite is significantly enhanced by the warm rolling treatment. This enhancement is attributed to the high dislocation density introduced by warm rolling. The complex role of dislocations on the austenite stability is rationalized based on the amounts of dislocations. Kajiwara *et al.*[30] reported that the presence of a small number of dislocations in austenite grain facilitates the nucleation of martensite by initiating the plastic accommodation of transformation strain of martensite, whereas a high dislocation density—forming dislocation cell networks—suppresses the nucleation due to the increased strength of austenite. Tsuzaki *et al.*[31] also reported that the austenite was strengthened by prior deformation and extra energy was required for the transformation dislocations to advance through forest dislocations in austenite matrix. The marked stabilization of pre-deformed austenite against the athermal γ-ε martensitic transformation is primarily attributed to the fact that the increase in the chemical driving force for transformation with decreasing temperature is less significant than the energy required to overcome dislocation-induced barriers. In this study, the athermal γ-ε martensitic transformation at 77 K was completely suppressed by the warm rolling treatment, whereas the deformation-induced γ-ε martensitic transformation remained active at room temperature, thereby resulting in high strength and large ductility.

To investigate the mechanical stability and yielding mechanism of the HR+WR specimen, an interrupted tensile test was performed, followed by postmortem XRD and EBSD analyses. The tensile specimen was loaded to 600 MPa and then unloaded. **Figure 9**(a) shows the magnified region taken from the nominal stress–strain curve of HR+WR specimen depicted in Fig. 4(a), highlighting the detailed behavior of the entire yielding stage. The nominal stress-strain curve exhibited a deviation from linearity at 600 MPa before 0.2% offset yield strength (621.5±0.5 MPa). This deviation indicated the occurrence of micro-yielding. Figure 9(b) shows the XRD profile of the HR+WR specimen subjected to the interrupted tensile test, revealing no distinct diffraction peaks corresponding to the ε-martensite. The EBSD mapping also confirmed that the specimen retained a single-phase austenite structure, as illustrated in Figs. 9(c) and 9(d). Both the XRD and EBSD analyses demonstrated that γ-ε martensitic transformation had not yet taken place. Consequently, the onset of plastic deformation in the HR+WR specimen is attributed to dislocation slip within the parent austenite phase rather than to stress-assisted martensitic transformation. The warm rolling treatment of the metastable HEA in the austenitic state enhanced the mechanical stability against stress-assisted γ-ε martensitic transformation, shifting the yielding mechanism from martensitic transformation to dislocation slip and resulting in an increase in yield strength. Furthermore, when the work-hardened austenite is deformed beyond the critical stress for martensite formation, the amount of martensite increases as deformation progresses, as shown in Figs. 6 and 7.

With respect to the superior mechanical properties of the metastable $Fe_{50}Mn_{30}Cr_{10}Co_{10}$ HEA at room tempera-

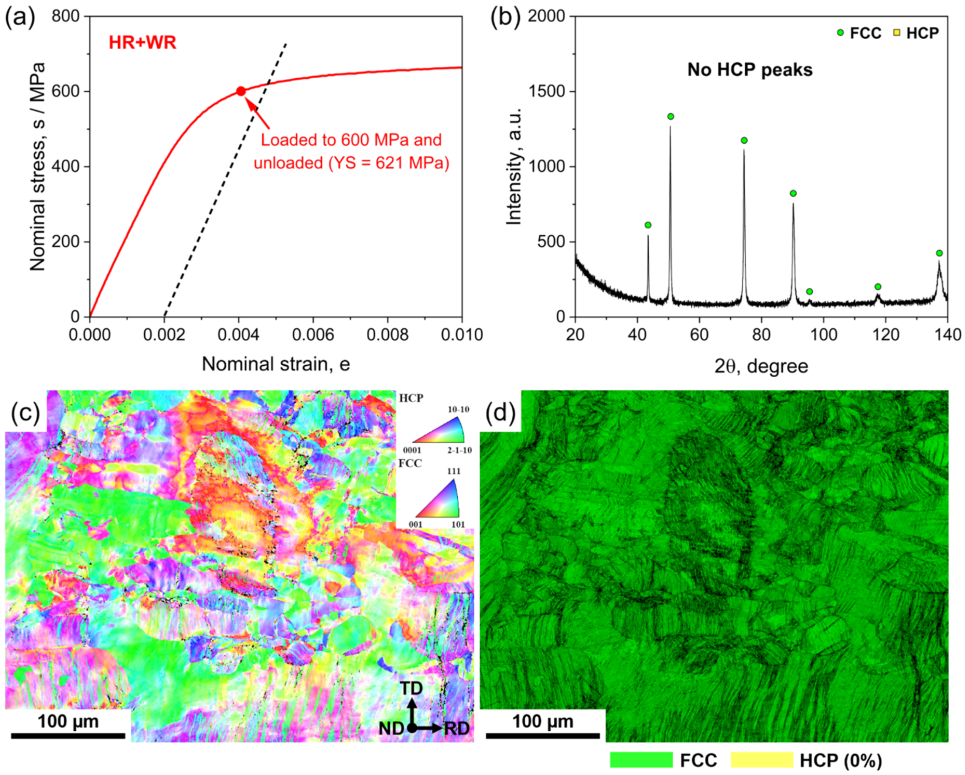

Fig. 9. (a) Enlarged nominal stress–strain curve of the HR+WR specimen showing the detailed behavior of the yielding stage; (b) XRD profile for the HR+WR specimen after the interrupted tensile test; (c) and (d) are the corresponding IPF map and IQ + phase map of the HR+WR specimen after the interrupted tensile test. (Online version in color.)

ture, a comparison of the yield strength versus uniform elongation with those of other FCC HEAs reported in the literature[2,3,13,21,32–40] is summarized in **Fig. 10**. The present HR+WR and ANN + WR specimens exhibit an exceptional combination of yield strength and uniform elongation compared to both the fully recrystallized counterparts and other single-phase FCC HEAs, making it a desirable alloy for applications where high yield strength and large ductility are critical design criteria. The outstanding mechanical performance of the HR+WR and ANN + WR specimens indicates that the direct warm rolling treatment could be a straightforward and cost-effective thermomechanical processing strategy: the metastable austenite is work-hardened and mechanically stabilized, which changes the yielding mechanism from martensitic transformation to dislocation slip while retaining the ε-TRIP effect after austenite yielding. Consequently, the warm-rolled metastable HEA exhibits significant potential for further improvement of mechanical properties considering the influence of warm rolling treatment on the work hardening of austenite and the ε-TRIP effect. By adjusting the warm rolling parameters, it may be possible to fine-tune the phase stability of austenite, thereby tailoring the alloy's strength–ductility balance to meet specific design requirements.

3.6. Future Study

The present study demonstrates that a 50% warm rolling treatment significantly enhances the yield strength of the metastable $Fe_{50}Mn_{30}Cr_{10}Co_{10}$ HEA while preserving substantial ductility. To explore this phenomenon in depth, we plan to conduct tensile tests combined with *in-situ* neutron diffraction to quantify the kinetics of the γ-ε martensitic transformation and its relationship with work hardening, clarifying the mechanisms underlying the observed strength–ductility synergy. In addition, the 50% warm rolling treatment completely suppresses the athermal γ-ε martensitic transformation during cooling to 77 K, while strain-induced martensitic transformation remains active at room temperature—resulting in both high strength and large ductility. These results also open two promising avenues for future research: (i) The effects of low-temperature hot deformation on austenite phase stabilization and ε-martensite variant selection. This fundamental study of the γ-ε martensitic transformation is critical for optimizing the microstructural design of metastable HEA through thermomechanical processing, potentially leading to further enhancements in mechanical performance. (ii) The mechanical performance and deformation mechanisms of warm-rolled metastable HEA at cryogenic temperatures. The warm-rolled metastable HEA holds considerable promise for achieving exceptional mechanical properties at cryogenic temperatures, as the thermally activated dislocation motion becomes increasingly difficult, and the reduced stacking fault energy promotes the phase transformation. A systematic investigation of the ε-TRIP effect and related deformation mechanisms is essential for developing high-performance alloys for cryogenic applications.

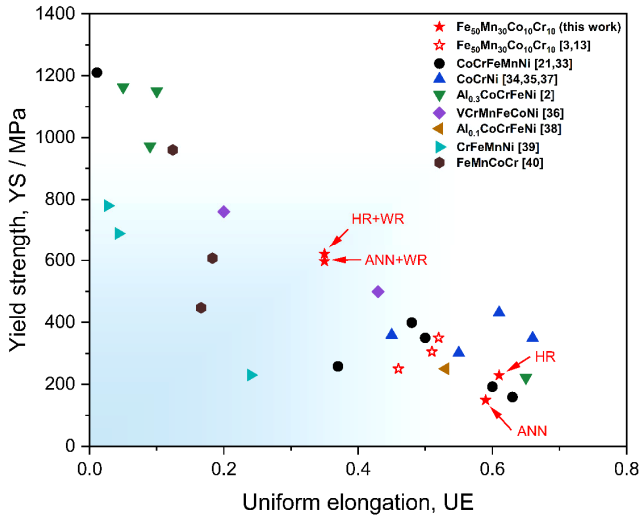

Fig. 10. Yield strength versus uniform elongation of the metastable $Fe_{50}Mn_{30}Cr_{10}Co_{10}$ HEA in comparison with those of other FCC HEAs reported in the literature. (Online version in color.)

4. Conclusions

In this study, we developed a straightforward and cost-effective thermomechanical processing strategy to fabricate metastable $Fe_{50}Mn_{30}Cr_{10}Co_{10}$ HEA with enhanced yield strength while retaining large ductility. The effects of 50% warm rolling treatment at 573 K (above the A_f temperature) on the mechanical properties of the metastable HEA and the ε-TRIP effect were investigated using room temperature tensile tests combined with postmortem XRD and EBSD analyses. The main conclusions are as follows:

(1) Compared to the ANN specimens, the HR+WR and ANN+WR specimens exhibited a threefold increase in yield strength (from 154.5±5.5 MPa to 621.5±0.5 MPa and 600±3 MPa, respectively) while maintaining substantial uniform elongations of 0.33±0.02 and 0.34±0.01. An excellent combination of strength and ductility was achieved in the HR+WR and ANN+WR specimens.

(2) The warm rolling treatment of the metastable HEA in austenitic state enhanced the mechanical stability against stress-assisted γ-ε martensitic transformation, shifting the yielding mechanism from martensitic transformation to dislocation slip and resulting in an increase in yield strength.

(3) The athermal γ-ε martensitic transformation was completely suppressed at 77 K by the warm rolling treatment, but the strain-induced γ-ε martensitic transformation remained significant at room temperature (f_{HCP}: 0% → 42.2%), contributing to both high strength and large ductility.

(4) Warm rolling above the A_f temperature could be a straightforward and cost-effective thermomechanical processing strategy to fabricate metastable HEA with enhanced yield strength while retaining large ductility, enabling industrial implementation with minimal changes to existing processes.

Declaration of Interests

The authors declare that they have no known competing financial interests or personal relationships that could have appeared to influence the work reported in this paper.

Acknowledgments

This research was financially supported by 32nd ISIJ

Research Promotion Grant. A part of this work was supported by “Advanced Research Infrastructure for Materials and Nanotechnology in Japan (ARIM)” of the Ministry of Education, Culture, Sports, Science and Technology (MEXT) under proposal number JPMXP1224NM5324. The authors express their sincere gratitude to Dr. Takanobu Hiroto (National Institute for Materials Science) for his support in conducting XRD analysis.

REFERENCES

1) Y. Zhang, T.T. Zuo, Z. Tang, M.C. Gao, K.A. Dahmen, P.K. Liaw and Z.P. Lu: *Prog. Mater Sci.*, **61** (2014), 1. https://doi.org/10.1016/j.pmatsci.2013.10.001
2) Y.H. Jo, S. Jung, W.M. Choi, S.S. Sohn, H.S. Kim, B.J. Lee, N.J. Kim and S. Lee: *Nat. Commun.*, **8** (2017), 15719. https://doi.org/10.1038/ncomms15719
3) Z. Li, K.G. Pradeep, Y. Deng, D. Raabe and C.C. Tasan: *Nature*, **534** (2016), 227. https://doi.org/10.1038/nature17981
4) B. Cantor, I.T.H. Chang, P. Knight and A.J.B. Vincent: *Mater. Sci. Eng., A*, **375**–**377** (2004), 213. https://doi.org/10.1016/j.msea.2003.10.257
5) S.W. Wu, G. Wang, J. Yi, Y.D. Jia, I. Hussain, Q.J. Zhai and P.K. Liaw: *Mater. Res. Lett.*, **5** (2017), 276. https://doi.org/10.1080/21663831.2016.1257514
6) T.H. Chou, W.P. Li, H.W. Chang, X.H. Du, W.S. Chuang, T. Yang, Y.T. Zhu and J.C. Huang: *Int. J. Plast.*, **159** (2022), 103482. https://doi.org/10.1016/j.ijplas.2022.103482
7) N. Tsuji, Y. Ito, Y. Saito and Y. Minamino: *Scr. Mater.*, **47** (2002), 893. https://doi.org/10.1016/S1359-6462(02)00282-8
8) R. Valiev: *Nat. Mater.*, **3** (2004), 511. https://doi.org/10.1038/nmat1180
9) Y. Wang, M. Chen, F. Zhou and E. Ma: *Nature*, **419** (2002), 912. https://doi.org/10.1038/nature01133
10) X.T. Fang, G.Z. He, C. Zheng, X.L. Ma, D. Kaoumi, Y.S. Li and Y.T. Zhu: *Acta Mater.*, **186** (2020), 644. https://doi.org/10.1016/j.actamat.2020.01.037
11) Y. Tong, D. Chen, B. Han, J. Wang, R. Feng, T. Yang, C. Zhao, Y.L. Zhao, W. Guo, Y. Shimizu, C.T. Liu, P.K. Liaw, K. Inoue, Y. Nagai, A. Hu and J.J. Kai: *Acta Mater.*, **165** (2019), 228. https://doi.org/10.1016/j.actamat.2018.11.049
12) B. Gludovatz, A. Hohenwarter, D. Catoor, E.H. Chang, E.P. George and R.O. Ritchie: *Science*, **345** (2014), 1153. https://doi.org/10.1126/science.1254581
13) Z. Li, C.C. Tasan, K.G. Pradeep and D. Raabe: *Acta Mater.*, **131** (2017), 323. https://doi.org/10.1016/j.actamat.2017.03.069
14) M.M. Wang, C.C. Tasan, D. Ponge and D. Raabe: *Acta Mater.*, **111** (2016), 262. https://doi.org/10.1016/j.actamat.2016.03.070
15) W. Mao, W. Gong, S. Harjo, S. Morooka, S. Gao, T. Kawasaki and N. Tsuji: *J. Mater. Sci. Technol.*, **176** (2024), 69. https://doi.org/10.1016/j.jmst.2023.07.036
16) C. Herrera, D. Ponge and D. Raabe: *Acta Mater.*, **59** (2011), 4653. https://doi.org/10.1016/j.actamat.2011.04.011
17) L. Chen, Z. Li, P. Dai, P. Fu, Q. Tang and J. Chen: *J. Alloys Compd.*, **955** (2023), 170225. https://doi.org/10.1016/j.jallcom.2023.170225
18) D. Li, Z. Li, L. Xie, Y. Zhang and W. Wang: *Nano Res.*, **15** (2022), 4859. https://doi.org/10.1007/s12274-021-3719-y
19) E.O. Hall: *Proc. Phys. Soc. London, Sect. B*, **64** (1951), 747. https://doi.org/10.1088/0370-1301/64/9/303
20) J. Petch N: *Journal of the Iron and Steel Institute*, **174** (1953), 25. https://cir.nii.ac.jp/crid/1570291225556359040
21) F. Otto, A. Dlouhý, C. Somsen, H. Bei, G. Eggeler and E.P. George: *Acta Mater.*, **61** (2013), 5743. https://doi.org/10.1016/j.actamat.2013.06.018
22) Z. Li, C.C. Tasan, H. Springer, B. Gault and D. Raabe: *Sci. Rep.*, **7** (2017), 40704. https://doi.org/10.1038/srep40704
23) N. Tsuji, S. Ogata, H. Inui, I. Tanaka, K. Kishida, S. Gao, W. Mao, Y. Bai, R. Zheng and J. Du: *Scr. Mater.*, **181** (2020), 35. https://doi.org/10.1016/j.scriptamat.2020.02.001
24) Y. Zhao, D.-H. Lee, W.-J. Kim, M.-Y. Seok, J.-Y. Kim, H.N. Han, J.-Y. Suh, U. Ramamurty and J.-i. Jang: *Mater. Sci. Eng., A*, **718** (2018), 43. https://doi.org/10.1016/j.msea.2018.01.107
25) S. Gao, Y. Bai, R. Zheng, Y. Tian, W. Mao, A. Shibata and N. Tsuji: *Scr. Mater.*, **159** (2019), 28. https://doi.org/10.1016/j.scriptamat.2018.09.007
26) G.B. Olson and M. Cohen: *Journal of the Less Common Metals*, **28** (1972), 107. https://doi.org/10.1016/0022-5088(72)90173-7
27) M. Koyama, T. Gondo and K. Tsuzaki: *Metals*, **11** (2021), 742. https://doi.org/10.3390/met11050742
28) Y. Bu, Z. Li, J. Liu, H. Wang, D. Raabe and W. Yang: *Phys. Rev. Lett.*, **122** (2019), 075502-1. https://doi.org/10.1103/PhysRevLett.122.075502
29) Z. Li, F. Körmann, B. Grabowski, J. Neugebauer and D. Raabe: *Acta Mater.*, **136** (2017), 262. https://doi.org/10.1016/j.actamat.2017.07.023
30) S. Kajiwara: *Metall. Trans. A*, **17** (1986), 1693. https://doi.org/10.1007/BF02817268
31) K. Tsuzaki, S. Fukasaku, Y. Tomota and T. Maki: *Mater. Trans., JIM*, **32** (1991), 222. https://doi.org/10.2320/matertrans1989.32.222
32) S.J. Sun, Y.Z. Tian, H.R. Lin, H.J. Yang, X.G. Dong, Y.H. Wang and Z.F. Zhang: *Mater. Sci. Eng., A*, **740**–**741** (2019), 336. https://doi.org/10.1016/j.msea.2018.10.094
33) G. Laplanche, A. Kostka, C. Reinhart, J. Hunfeld, G. Eggeler and E.P. George: *Acta Mater.*, **128** (2017), 292. https://doi.org/10.1016/j.actamat.2017.02.036
34) B. Gludovatz, A. Hohenwarter, K.V.S. Thurston, H. Bei, Z. Wu, E.P. George and R.O. Ritchie: *Nat. Commun.*, **7** (2016), 10602. https://doi.org/10.1038/ncomms10602
35) D. Li, C. Li, T. Feng, Y. Zhang, G. Sha, J.J. Lewandowski, P.K. Liaw and Y. Zhang: *Acta Mater.*, **123** (2017), 285. https://doi.org/10.1016/j.actamat.2016.10.038
36) J. Miao, C.E. Slone, T.M. Smith, C. Niu, H. Bei, M. Ghazisaeidi, G.M. Pharr and M.J. Mills: *Acta Mater.*, **132** (2017), 35. https://doi.org/10.1016/j.actamat.2017.04.033
37) D. Li and Y. Zhang: *Intermetallics*, **70** (2016), 24. https://doi.org/10.1016/j.intermet.2015.11.002
38) J.G. Gigax, O. El-Atwani, Q. McCulloch, B. Aytuna, M. Efe, S. Fensin, S.A. Maloy and N. Li: *Scr. Mater.*, **178** (2020), 508. https://doi.org/10.1016/j.scriptamat.2019.11.042
39) G. Li, M. Liu, S. Lyu, M. Nakatani, R. Zheng, C. Ma, Q. Li and K. Ameyama: *Scr. Mater.*, **191** (2021), 196. https://doi.org/10.1016/j.scriptamat.2020.09.036
40) Z. Wu, H. Bei, G.M. Pharr and E.P. George: *Acta Mater.*, **81** (2014), 428. https://doi.org/10.1016/j.actamat.2014.08.026